

On-sky performance of SPIFFI: the integral field spectrometer for SINFONI at the VLT

Christof Iserlohe^a, Matthias Tecza^b, Frank Eisenhauer, Reinhard Genzel^c, Niranjan Thatte^d,
Roberto Abuter, Matthew J. Horrobin, Alexander Schegerer^e, Jürgen Schreiber^f,
Henri Bonnet^g

Max-Planck Institut für extraterrestrische Physik, Garching, Germany

^asince January 2004 1. Physikalisches Institut der Universität zu Köln, Germany

^bsince January 2004 Department of Astrophysics, University of Oxford, U.K.

^calso Department of Physics, University of California, Berkeley, USA

^dsince April 2003 Department of Astrophysics, University of Oxford, U.K.

^euntil January 2004 Max-Planck Institut für extraterrestrische Physik, Garching, Germany

^fsince January 2004 Max-Planck Institut für Astronomie, Heidelberg, Germany

^gEuropean Southern Observatory, Garching, Germany

ABSTRACT

SPIFFI (**SP**ectrometer for **I**nfrared **F**aint **F**ield **I**maging) is a fully cryogenic, near-infrared imaging spectrograph built at the Max-Planck-Institute for Extraterrestrial Physics (MPE) and upgraded with a new detector and spectrograph camera by ASTRON/NOVA, ESO and MPE. The upgraded instrument will become a facility instrument for the ESO VLT in summer 2004 as part of the SINFONI (**S**INgle **F**aint **O**bject **N**ear-**I**R **I**nvestigation) project, which is the combination of SPIFFI and ESOs adaptive optics module MACAO (**M**ultiple **A**pplication **C**urvature **A**daptive **O**ptics), at the Cassegrain focus of Yepun (UT4). In spring 2003 we had the opportunity to observe with SPIFFI as a guest instrument without the AO-module at the Cassegrain focus of UT2 of the VLT. In this paper we discuss the performance of SPIFFI during the guest-instrument phase. First we summarize the technical performance of SPIFFI like the spatial and spectral resolution, the detector performance and the instruments throughput. Afterwards we illustrate the power of integral field spectroscopy by presenting data and results of the Galactic Center.

1. INTRODUCTION

An integral field spectrograph allows the observer to obtain spectra for each spatial element of the field of view of the instrument. Classical techniques like Fabry-Perot interferometers or slit scanning techniques are time consuming and therefore not immune against effects related to the strongly varying atmospheric emission in the near-infrared. Besides calibration problems, the interpretation of data of complex objects can be difficult when the object is only investigated partially. For example determinations of the underlying dynamics of complex interacting systems can result in ambiguities especially when the dynamical properties are only known along a few slits. With integral field spectroscopy these ambiguities can be eliminated effectively.

SPIFFI^{4,5} allows simultaneous spectroscopy of 1024 pixels in a 32×32 pixel field-of-view resulting in a data cube with two spatial and one spectral axis. SINFONI, the combination of SPIFFI with the adaptive optics module MACAO², will perform imaging spectroscopy with a diffraction limited angular resolution of about $0.05''$. The instrument covers a wavelength range from $1\mu\text{m}$ to $2.45\mu\text{m}$, providing a spectral resolving power ranging from $R=1000$ to 4000. Equipped with interchangeable optics, SPIFFI can be operated with a pixel scale of $0.250''$ and $0.100''$ in seeing limited and $0.025''$ in AO-assisted mode (corresponding to a field-of-view of $8'' \times 8''$, $3.2'' \times 3.2''$ and $0.8'' \times 0.8''$ respectively).

2. THE INSTRUMENT

The light enters the instrument at the Sky-spider device (S) (see Figure 1). This device consists of a plane mirror system which allows to redirect light from a distance of up to $45''$ from the target into the instruments field-of-view. The purpose is to allow simultaneous observations of extended objects and the night sky emission to avoid overheads from separate sky observations. After the pre-optics collimator (PC) the light passes the filter wheel (F) and the pre-optics wheel (PO) which provides the different pixel scales of $0.250''$, $0.100''$ and $0.025''$ per pixel. The pre-optics reimages the object plane onto the image slicer¹⁶ (S), which cuts the two dimensional field into stripes and rearranges them to form the pseudo-slit (see Figure 2). Collimation is provided by a mirror collimator which consists of three diamond turned and post-polished mirrors (C1-3), one spherical mirror and two oblate ellipsoidal off-axis mirrors. One of four gratings (G) (one for the J-, H-, K, and H+K-Band respectively) disperses the light and reflects it into a fast $f/1.4$ camera (C) using glass (IRG2) and crystal (BaF_2) lenses. The dispersed pseudo-slit covers exactly a HAWAII $1k \times 1k$ chip (D) from Rockwell Industries. Because of the various peculiarities of the raw data from integral field spectroscopy SPIFFI has its own data reduction software¹⁵. This software package provides all tools for the calibration and reduction of SPIFFI data, including wavelength calibration and image reconstruction. The final data format is a three-dimensional data cube with 32×32 spatial pixels, and up to 2560 spectral elements, in case of spectral dithering. To obtain Nyquist sampled spectra it is necessary to shift the spectra by $1/2$ a detector pixel in spectral direction by turning the grating wheel between consecutive integrations. This method, referred to as spectral dithering, results in spectra that have twice as many resolution elements as undithered spectra.

The upgraded instrument will have a 2048×2048 pixel Rockwell HAWAII 2 RG detector and a new $f/2.8$ camera which will allow to obtain Nyquist sampled spectra in one integration. The upgrade is a joint effort by ASTRON/NOVA, ESO and MPE.

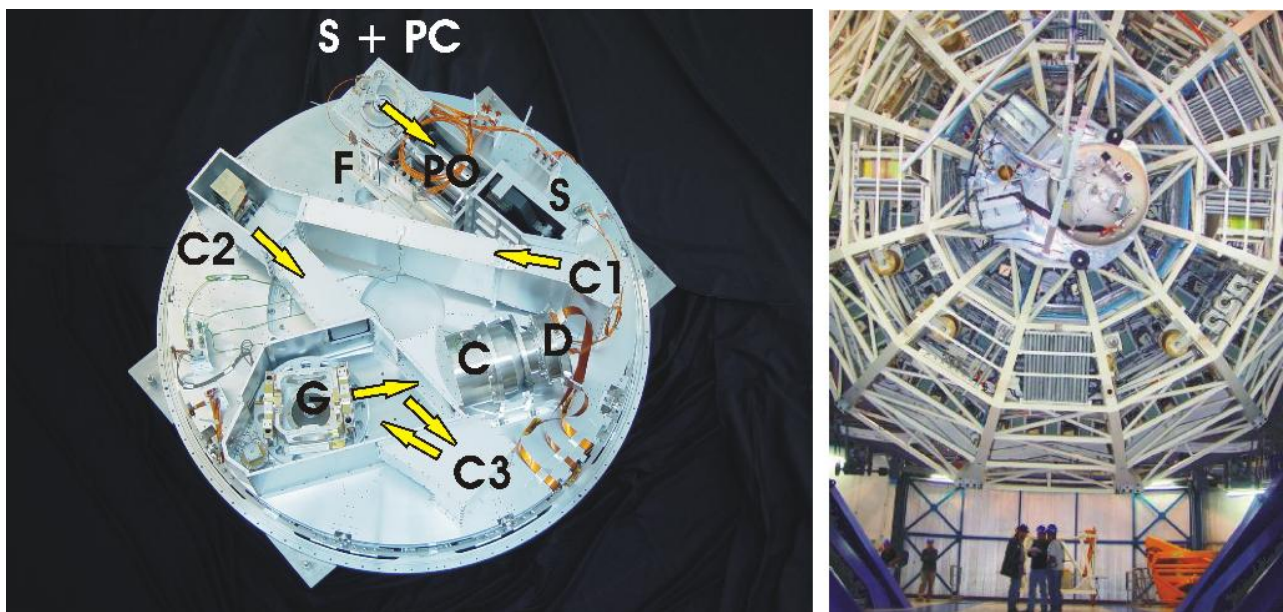


Figure 1. Left: Mechanical and optomechanical components mounted to the baseplate (see text). The arrows indicate the lightpath. The letters are explained in the text. Right: SPIFFI mounted to the Cassegrain focus of UT2 pointing to the horizon. The cryostat is mounted to the Cassegrain derotator with an interface flange to which the electronic racks and the calibration unit are attached.

3. IMAGE QUALITY

Pre-optics system: The spatial resolution of the instrument depends mostly on the image quality of the pre-optics system which reimages the object plane onto the small image slicer. To measure the image quality a

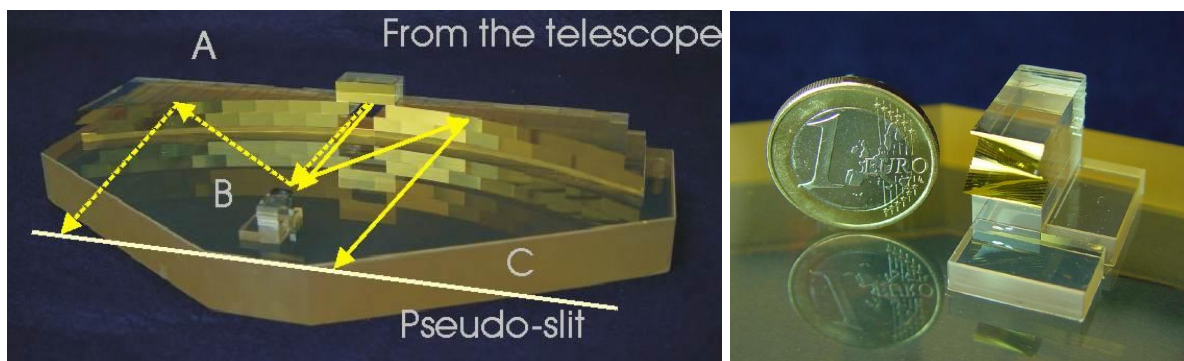


Figure 2. The image slicer: The image slicing device used in SPIFFI consists of plane mirrors. The two dimensional image (still containing light of all wavelengths of the used observing band) is sliced into thin stripes, called slitlets, which are then lined up end to end to create a pseudo long slit which is fed into the spectrometer. The small image slicer (B in left Figure) is a stack of 32 plane mirrors with a thickness of 0.3mm each. The small image slicer (right Figure) cuts the image into stripes and reflects them onto the big image slicer (A) which consists of 32 plane mirrors in two layers. The mirrors are tipped and tilted in a way that the telecentric entrance pupil is preserved. Both image slicer components are mounted to a baseplate(C). All parts are of Zerodur and are optically contacted (without using any glue).

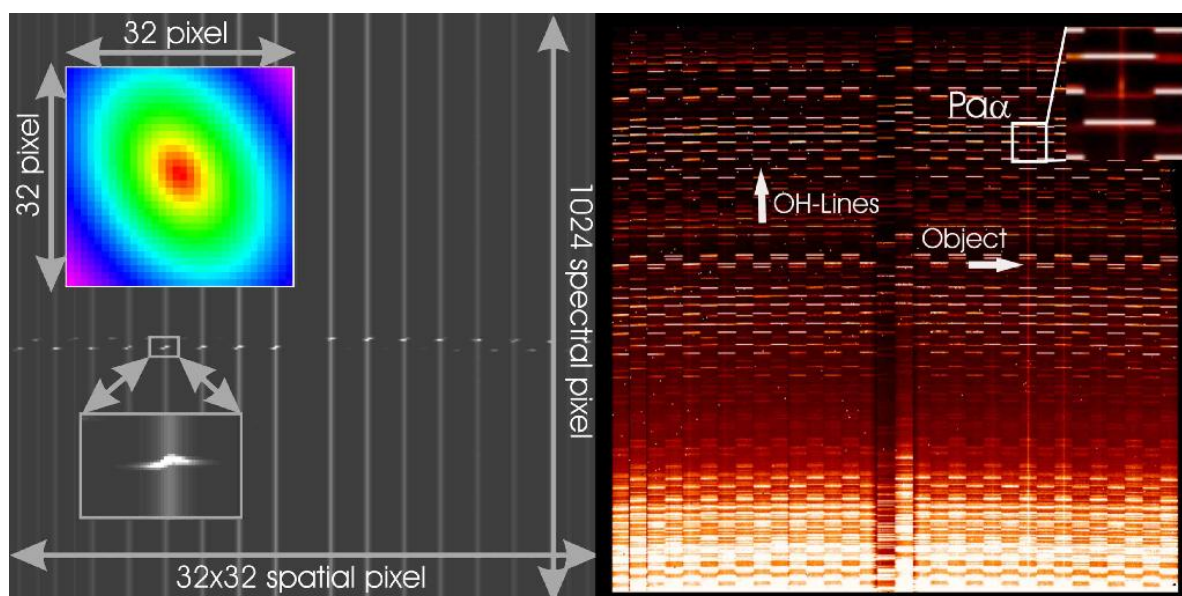


Figure 3. Left: Simulated image of a rotating source with continuum and one emission line. Each slitlet is 32 columns wide on the detector and with 32 slitlets one obtains 1024 spatial pixels with each spectrum covering exactly one detector column. The inset to the upper left shows the reconstructed image after having rearranged the slitlets. The inset below shows the velocity dispersed emission line. Right: K-band detector raw frame of the ULIRG IRAS06206-6315. Together with bright night skylines (mainly OH), thermal atmospheric background, continuum and line emission of the source can be identified (long wavelengths at the bottom). The inset shows Pa_α line emission.

teststand has been designed with the slicer being replaced by the detector to obtain higher spatial sampling of the pre-optics PSF than in the complete instrumental setup. Figure 4 shows the measured and theoretical pre-optics PSF in H-band using the 0.100" pixel scale. The theoretical and measured PSFs are in very good agreement in terms of encircled energies. Also the achieved Strehl ratios for all bands and pixel scales are greater than 90%.

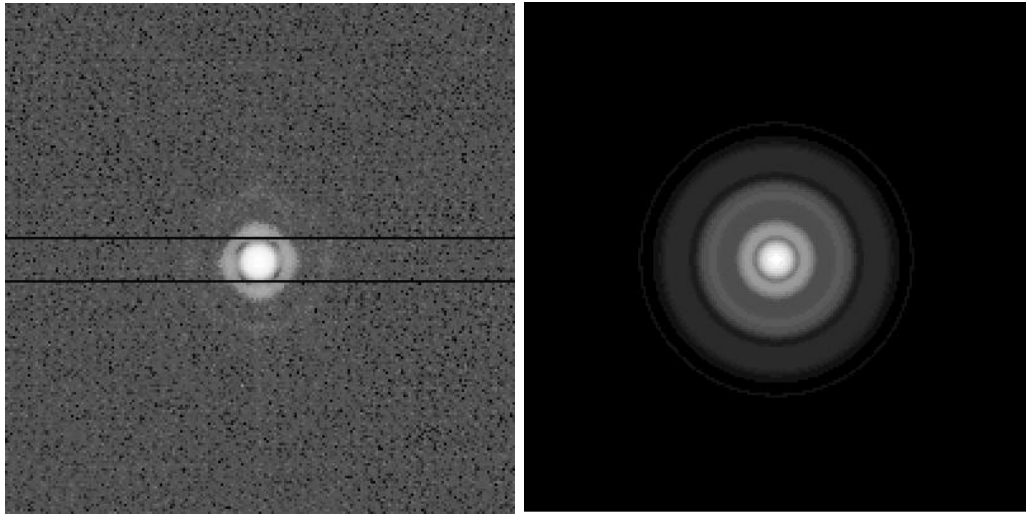


Figure 4. Results from the pre-optics test. Top: Measured (left) and theoretical (right) PSF of the pre-optics system in H-band using the 0.100" pixel scale. The two black bars in the left figure indicate the width of a single mirror of the small image slicer.

SPIFFI spectrograph camera: Crucial for the spectral resolution is the image quality of the spectrometer camera (see Figure 5, left). Before SPIFFI was brought to the telescope we measured interferometrically wavefront aberrations that are introduced by the spectrograph camera in Garching. The teststand consists of a μ Phase150 laser interferometer (633nm) from Fisba, the spectrograph camera and a return sphere. The wavefront aberrations are measured in double pass mode with a collimated beam of 150mm in diameter at ambient temperature. To correct effects due to the red laser light and the difference in operating temperature a null lens has been placed in front of the camera. The camera lenses are assembled in four subunits which can be rotated in 30° increments around the optical axis. The distance between these units can be changed with spacers of 0.2mm thickness.

The image quality of the spectrograph camera subunits has been characterized in terms of Seidel aberrations. The lower order angular dependent wavefront aberrations, have been determined by rotating the subunits by 90° (see Table 1).

Unit	Astigmatism [nm]	Direction [degree]	Coma [degree]	Direction [degree]
4	13	-61	107	76
3	372	-26	262	85
2	104	38	233	74
1	259	-18	50	-95

Table 1. Lower order angular dependent Seidel aberrations introduced by individual subunits of SPIFFI's spectrograph camera.

Astigmatism and coma have been reduced successfully by rotating subunit two and three by -90°. Spherical aberration has not been measured for the individual subunits of the camera; we have tried to correct for spherical aberrations by changing the separation of the individual subunits, but the net-effect was too small; we thus just changed the lens separation only to adjust the back focal distance. After the optimization process the best wavefront that we have measured is shown in Figure 5 (right). In this configuration the deduced rms spot size radius is smaller than 5 μ m and therefore within the design limits.

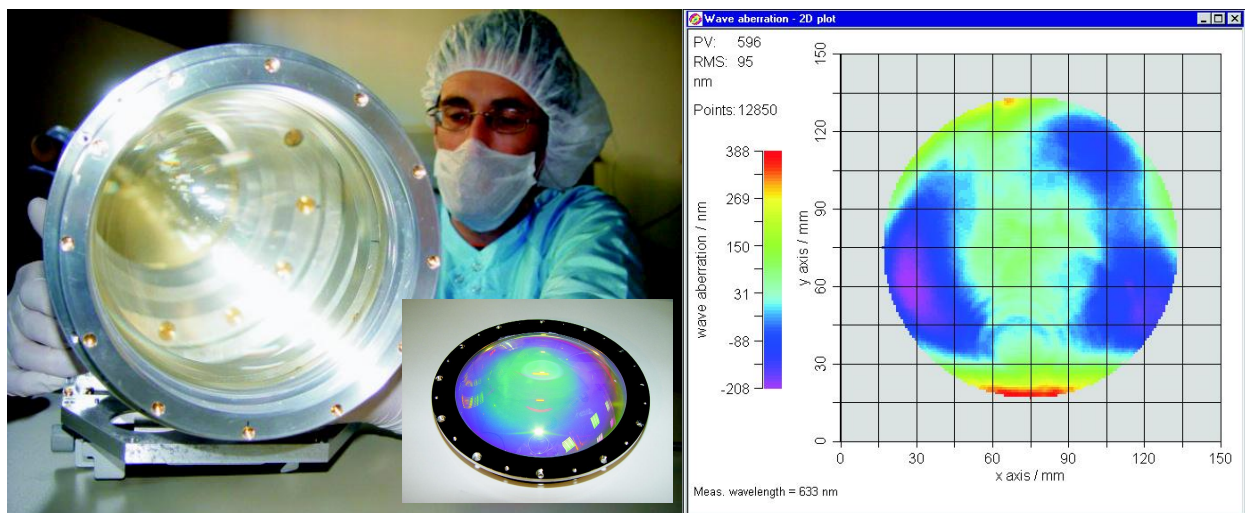


Figure 5. Left: Assembled spectrograph camera with the null lens. The lenses have been coated with an anti reflection coating after the interferometrical test, because the coating is opaque for red wavelengths. The inset shows subunit 1 with the coated front lens having a diameter of 15cm. Right: Best interferometrically measured wavefront deformation of SPIFFI's spectrograph camera. The ring-like structure at the bottom of the interferogram is related to internal reflections in the interferometer.

Residual spatial curvature of spectra: Intrinsically the spectra are curved in spatial (and spectral) direction on the detector. The reflection gratings are operated in Ebert configuration resulting in a symmetrical pillow-shaped distortion of 1.5 detector pixel at the detector edges. The spectrograph camera introduces a barrel-shaped distortion which straightens the spectra in spatial direction. With the external calibration unit of SPIFFI it is possible to reimagine a fine slit perpendicular onto the mirrors of the small image slicer. With this so-called North-South-test a continuum source illuminates the slit resulting in 32 continuum spectra. From these the straightness of the spectra have been measured by determining the center of intensity in each spectral channel. The residual curvature is found to be less than 2/10th of a detector pixel at the edge of the detector in all bands.

Spectral resolution: The spectral resolving power of the complete instrument has been determined from lab measurements using arcline frames used for wavelength calibration and bright distinct OH-lines from sky observations. The spectral profile depends strongly on the observing band. In H- and especially in K-band the profile can be approximated by a Moffat function, resembling the theoretically expected profile, while in J-band aberrations smear the profile such that it can be described better by a gaussian (see Figure 6). The FWHM of a spectral line ranges from about 1.5 resolution elements (spectrally undithered) in K-band, corresponding to a spectral resolution of $R = \lambda / \Delta\lambda \simeq 3300$, to about 2.2 resolution elements (spectrally undithered) in J-band ($R \simeq 2000$) when using the 0.250" pixel scale (see Figure 6). Generally the spectral resolution increases when using smaller pixel scales. In this case the diameter of the spectrograph entrance beam becomes smaller indicating that the spectrograph camera contributes to the total amount of aberrations. The different average resolutions in H and K band (Figure 6) indicate that the spectrograph camera suffers from axial color that could not have been detected with our interferometrical tests. The curvature within an observing band (Figure 6 top right) is only partially related to axial color. Measurements with smaller pixel scales resulting in a slower beam at the detector show less curvature indicating a tip and/or tilt of the detector with respect to the instruments focal plane. The defocus of the detector can be determined by taking two exposures, one with the left third the other with the right third of the instruments pupil being illuminated by an arclamp. Shifts of arclamp lines between these two exposures are proportional to the defocus of the detector revealing axial color and a small tilt of a few ten microns. Refocusing the detector to the best common focus improves the spectral resolution in H-band on cost of

the resolution in K-band but without a significant improvement in J-band (see below). In contradiction with the good results obtained from our interferometrical tests and the lack of significant improvements in J-band when refocusing the detector other possible sources of aberrations like the mirror collimator have been investigated. The collimator mirrors are made of nickel coated aluminium blanks. The aluminium blanks are returned to give them their initial shape and galvanically coated with a 150 μm nickel layer. Afterwards the mirrors have been diamond turned, postpolished and gold coated. The first mirrors that we received have been refurbished after it turned out that their surface quality has been out of specification. Two mirrors have been post polished by Carl Zeiss, Oberkochen, Germany and another mirror has been diamond turned again by LFM in Bremen, Germany (LFM: Labor für Mikrozerspanung). After this process the wavefront deformations introduced by the mirror collimator have been measured interferometrically and are found to be smaller than one would expect theoretically from the observed smearing. Finally after having tested the instrument with the new spectrograph camera in February-April 2004 it turned out that the decrease of performance in J-band comes from the bad surface quality of the J-band grating.

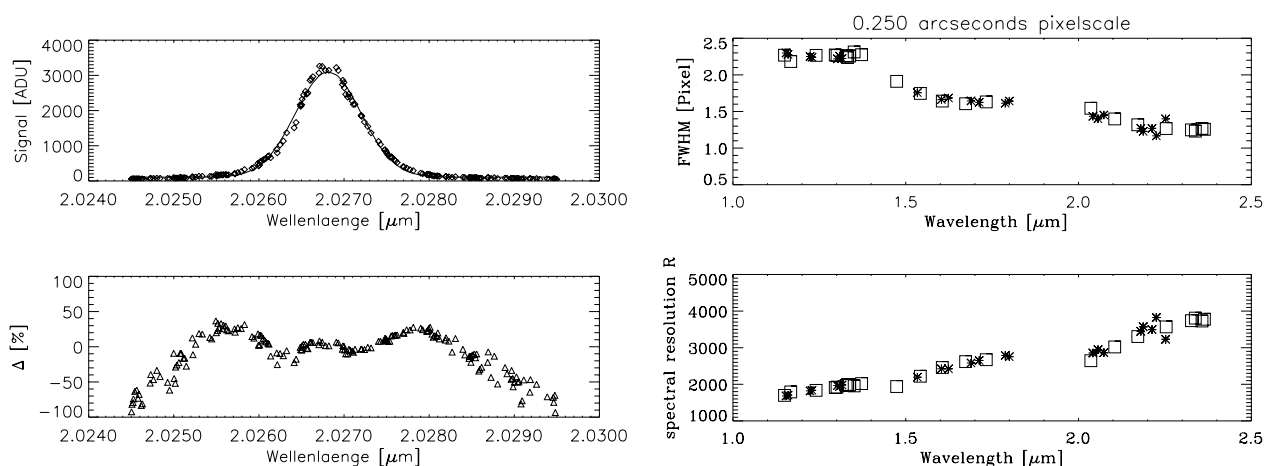


Figure 6. Left: Supersampled spectral line profile in K-band (top) and relative deviation of the line profile from a gaussian (bottom). Right: FWHM of measured emission lines (Ne, Ar, Xe (squares) and OH (stars)) (top) and spectral resolution R (bottom) as a function of wavelength for the 0.250" pixel scale.

4. DETECTOR

In its guest instrument phase, SPIFFI used a HAWAII 1k \times 1k detector from Rockwell Industries. These arrays are characterized by a high quantum efficiency in the NIR and a low darkcurrent. The read-out and control electronics used is ESOs IRACE system¹³ which is designed to have a low readout noise.

Detector model: SPIFFI's detector chain has been characterized in terms of darkcurrent, shiftregister glow* and readout noise⁷ (see Figure 7). Formally the total detector noise N can be expressed by

$$N = \sqrt{\frac{r^2}{NDS} + s * NDS + d * t} \quad (1)$$

(with the readout noise r of a double correlated readout, the shiftregister glow s, the highly temperature dependent darkcurrent d, the number of double correlated readouts NDS and the effective integration time t) with an

*The HAWAII-FPAs are equipped with on-chip preamplifiers that cause a strong glow. In SPIFFI they are not used, the preamplification takes place on the detector board instead. Only the glow of the shiftregisters contributes linearly with the number of reads to the total glow.

increasing number of readouts reducing the total detector noise⁸ and the shift register glow working against this trend. The values for s , d , and r have been determined by independent measurements and by measuring the total detector noise as a function of NDS and fitting the above equation to these data points (see Figure 7). Both methods consistently yield a detector darkcurrent of 0.27 electrons per second (at 78.2K), a readout noise of app. 18.1 electrons per double correlated read and a shiftregister glow of 0.6 electrons per double correlated read.

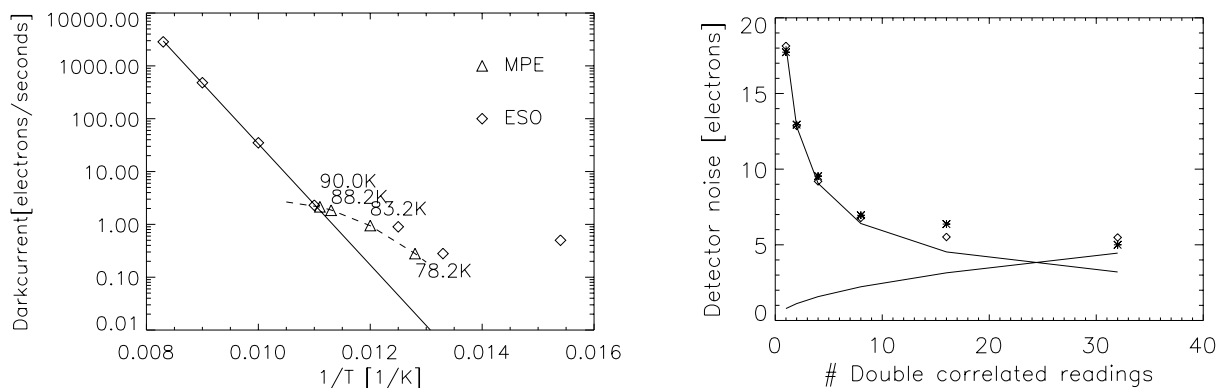


Figure 7. Left: Temperature dependence of the darkcurrent measured with the SPIFFI detector (triangles) and an ESO HAWAII 1k-chip (diamonds)⁷ Right: Darkcurrent subtracted readout noise in electrons as a function of double correlated readouts. Diamonds represent the measured noise values, stars the fitted values. The decreasing curve represents the decrease of readout noise corresponding to multiple readouts of the detector, the increasing curve the increasing contribution of the shiftregister glow.

Odd-even effect: The detector system suffers from the odd-even effect which causes different signal levels in odd and even columns. The effect is not constant in time and flux dependent. During commissioning we measured flux variations due to the odd-even effect of up to 5%. The origin of this effect is barely understood but can be minimized either in the obtained frames by masking out the one pixel in fourier space that represents a spatial frequency of one pixel[†] or by clocking the detector more slower. Both methods reduce the odd-even effect by 80%.

Fringing: The HAWAII-FPA uses a thin sapphire layer as detector substrate. This layer causes interference patterns (“fringes”) increasing in strength the slower the beam is at the detector. As seen in flatfield images this pattern causes intensity variations of several percent with a wavelength dependent periodicity of several resolution elements. Flexures of the instrument can cause shifts of the instruments focal plane on the detector (see below) shifting this pattern along the axis of dispersion. For this reason flatfielding of the instrument when using the 0.100” and especially the 0.025” pixel scale is difficult. To cope with this problem various flatfields with different grating settings have been obtained. For data reduction the appropriate ones must be selected. In that case the instrument has been successfully flat-fielded to up to 1%.

5. FLEXURES

Cassegrain instruments experience during observations a time dependent gravity load. Such instruments need to be either very stiff[‡] and/or their flexures need to be controlled with high accuracy. For this purpose two metrology sensors in SPIFFI determine the lateral displacement of the entrance beam with respect to the instruments field-of-view. This displacement is corrected with an appropriate telescope offset. Flexure contributions that are

[†]using the isaacp procedure of the Eclipse library³

[‡]To enforce the instruments stiffness a rigid aluminium structure has been attached to the coldplate of the cryostat which is not shown in figure 1.

not recognized by this device cannot be corrected and can cause a time dependent spatial sampling when the optical alignment before the image slicer is deformed (residual image motion) or a time dependent wavelength calibration (spectral shifts).

Residual image motion: Residual image motions of the instrument including the influence of the interface flange and the electronic racks have been measured with ESOs Cassegrain simulator in MPEs integration hall. A lens optics reimages a point source into the instruments focus which is inside the cryostat. The position of the point source in the collapsed data cube image with the instrument pointing to various zenith angles (of up to 68°) and rotator angles has been traced and compared to the metrology sensor data. Figure 8 (left) shows the deviation of the traced positions from a linear fit to the metrology sensor data. This residual image motion is less than 1/8th (rms) of a spatial element in AO-mode[§]. The residual image motion rate is less than 2μm per observing hour (a change of the zenith angle of 15°).

Spectral shifts: Spectral shifts or spectral flexures can occur if the grating wheel, the collimator mirrors or the camera bends during an integration. The measurement has been performed during daytime at Paranal observatory. The dependence of the shift S in resolution elements can be approximated by $S = 0.66 \times \sin(Z) \times \sin(R + 42.6^\circ)$ with Z being the zenith angle and R being the rotator angle of the Cassegrain derotator. Figure 8 (right) shows the measured and fitted shift as a function of rotator angle for a zenith angle of 45°. The maximum shift for a one hour integration (a change of the zenith angle of 15°) for zenith angles less than 60° is of the order of 1/10 resolution element (spectrally undithered).

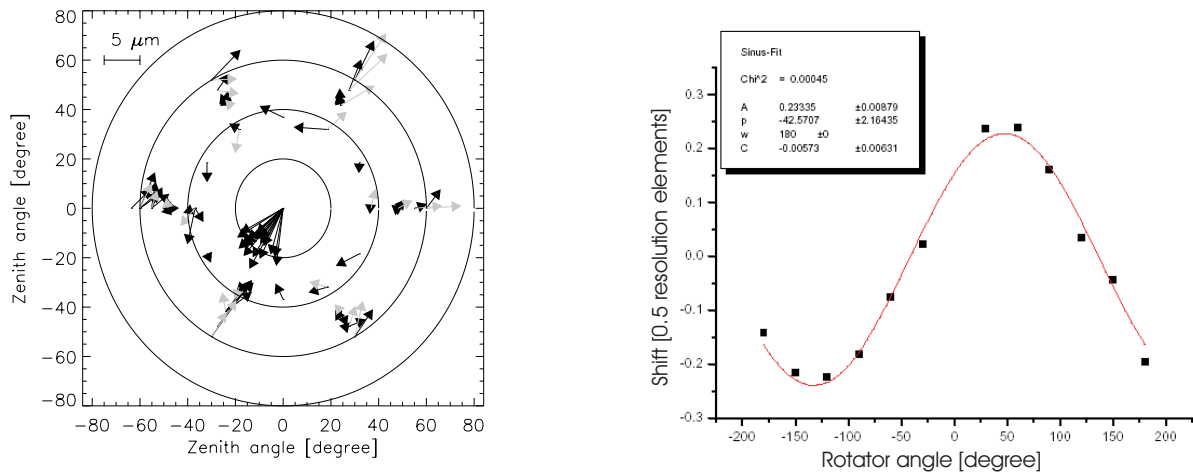


Figure 8. Left: Residual image motion in the reconstructed image as a function of azimuth and zenith angle. Dark/bright arrows indicate values taken after positive/negative Cassegrain derotator movements. Right: Spectral shift in half resolution elements for a zenith distance of 45° as a function of rotator angle.

6. EFFICIENCY AND LIMITING MAGNITUDES

The total efficiency of SPIFFI was determined from observations of photometric calibration stars. We define the efficiency as the ratio of detected photo electrons at the detector over the number of photons impinging at the instruments entrance window. Data for the efficiency calculation were taken with the 0.25" pixel scale and reduced using the SPIFFI data reduction software without flat field correction. The atmospheric transmission was calculated using the ATRAN¹ atmospheric modelling program. The adopted detector conversion factor was 3.4 e⁻/ADU. The efficiency (without the telescopes transmission) is found to be 24%, 39%, 40% in J-, H- and K-band respectively (see Figure 9).

[§]where a lateral displacement of 13μm causes a shift of one spatial element in the reconstructed image.

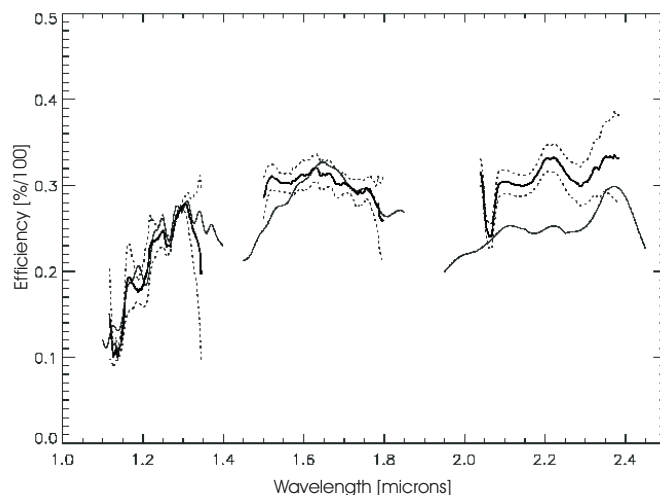


Figure 9. Efficiency (including the telescopes transmission) as a function of wavelength (see text). The solid bold line represents the average efficiency deduced from many atmospheric calibration stars, the dashed lines the 1σ uncertainties of the measurements. The solid line represents the efficiency deduced from measured/modelled filter transmission curves, transmission of optical elements, a telescope transmission of 79% and a detector quantum efficiency of 75%. Given the good agreement between the modelled and measured efficiencies, the manufacturer quoted detector quantum efficiency of 48% seems to be unreasonably low. The higher actual efficiency in K band may be explained by a higher transmission of the telescope and/or a higher detector quantum efficiency at longer wavelengths.

We have fed the SPIFFI Exposure Time Calculator (ETC) with the above values to determine limiting magnitudes for extended sources (see Table 2).

Scale [arcsec per pixel]	J [mag/arcsec ²]	H [mag/arcsec ²]	K [mag/arcsec ²]
0.250	18.7	18.0	16.8
0.100	17.2	16.9	15.8

Table 2. Limiting magnitudes for extended sources. The following assumptions were made: 6 exposures of 600 seconds each with 8 double correlated readouts, signal-to-noise ratio of 5, detector read noise of 18.1 electrons per double correlated readout and a darkcurrent of 0.27 electrons per second, average atmospheric, telescope and SPIFFIs transmission of 89%, 94%, 93% / 79%, 79%, 79% / 24%, 39%, 40% in J-, H- and K-band respectively, a telescope temperature of 283K (emissivity of 21%) (in K-band only), and a pixel scale of 0.250" per pixel, 0.100" per pixel. The average sky brightness in the individual bands is assumed to be 16.2, 14.3, 12.8 mag/arcsec².

7. STARE MODE

In the NIR regime the sky background is dominated by bright emission from OH-lines and/or thermal background (e.g. $K_{Sky} \simeq 13$ mag/arcsec²). Therefore it is inevitable to subtract this background from the object frame. The sky can be extracted from the science frame if the object is small compared to the field-of-view (stare mode) or when using the sky-spider device. The accuracy of the wavelength calibration is critical for this method. The standard wavelength calibration of the SPIFFI data reduction pipeline recovers the true position of a spectral line with an accuracy of about 1/10th (RMS) of a resolution element. Subtracting the sky with an extracted medianed sky spectrum results in strong residuals at the position of the OH-lines, that are typically stronger by a factor of 3 than the optimal poisson noise. Improvements of the pipeline wavelength calibration are still under investigation. Therefore the stare mode is not supported yet.

8. INTEGRAL FIELD SPECTROSCOPY OF THE GALACTIC CENTER STAR CLUSTER

The central region of our galaxy is highly obscured in the visible ($A_V \simeq 30$). Near-infrared integral field spectroscopy with SPIFFI allows one to look deep at the heart of our galaxy due to the lower extinction in the NIR ($A_{NIR} \simeq 3$) with the advantages of spatially high sampled spectroscopy. This allows us to investigate the properties, dynamics and evolution of stars and starclusters in the vicinity of a supermassive black hole. We have mosaiced during two nights (with a total integration time of 2 hours) the central region of $30'' \times 35''$ in H+K-band ($R \simeq 1300$, $\text{FWHM} \simeq 0.75''$) and the inner region of $6''$ in K-band ($R \simeq 3500$, $\text{FWHM} \simeq 0.3''$) providing us with the deepest and highest resolution imaging spectroscopy data set obtained up to this time.

Stellar content: From this dataset it has been possible to determine the stellar content of this region^{12,14,9,10} as seen in Figure 10. As an example, the simultaneous H+K capability allows us to unambiguously distinguish moderately late type (K2-5) supergiants from AGB stars. These data finally settle a long debate about the properties of the brightest late type stars in the central parsec: of the dozen or so $K < 10.5$ late type stars ($M(K) < -7.2$), a maximum of two are supergiants, the rest are clearly AGB stars.

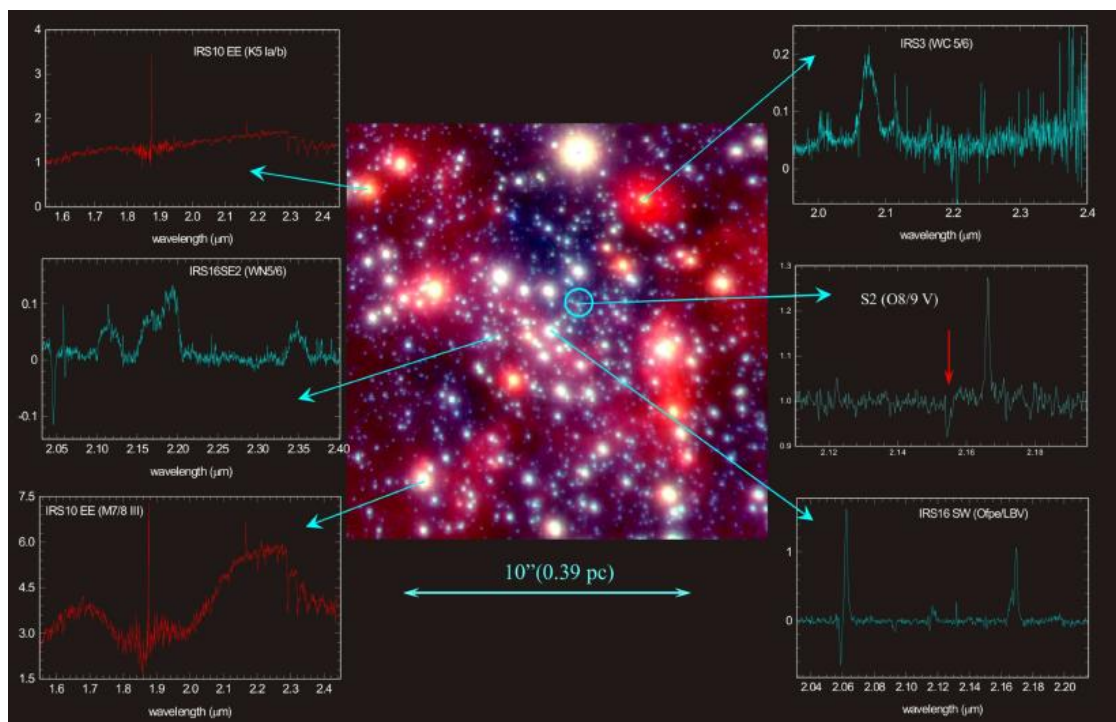


Figure 10. Selected spectra (corrected for atmospheric absorption but not for interstellar extinction) superposed on a NACO H/K/L color composite image of the central region. The spectra display the wide range of stellar types found in the cluster, ranging from late type main sequence O stars (the star S2 near SgrA*, oval in image), to luminous blue variables (IRS16SW, lower right), early WN (middle left) and WC (top right) Wolf-Rayet stars, to red supergiants (the brightest star IRS7 at the top/middle of the image), bright asymptotic giant branch stars (IRS9, lower left) and normal red giants (top left). The strong emission spike at $1.87\mu\text{m}$ is the H I Pa α recombination line in the H II region.

The Minispiral: A still ongoing analysis deals with the morphology and dynamics of gas flows, the “Minispiral”, around the central black hole, SgrA*. Ionized gas in this region has been traced with the infrared fine-structure line emission of [NeII] at $12.8\mu\text{m}$ and with the recombination line H 92α at 3.6cm . With the SPIFFI dataset it is possible to trace these gasflows in Br γ ($2.166\mu\text{m}$) (see Figure 11) and HeI. With the light collecting power of an 8-meter class telescope it has also been possible to map this region from the ground for the first time in Pa α (see Fig. 10).

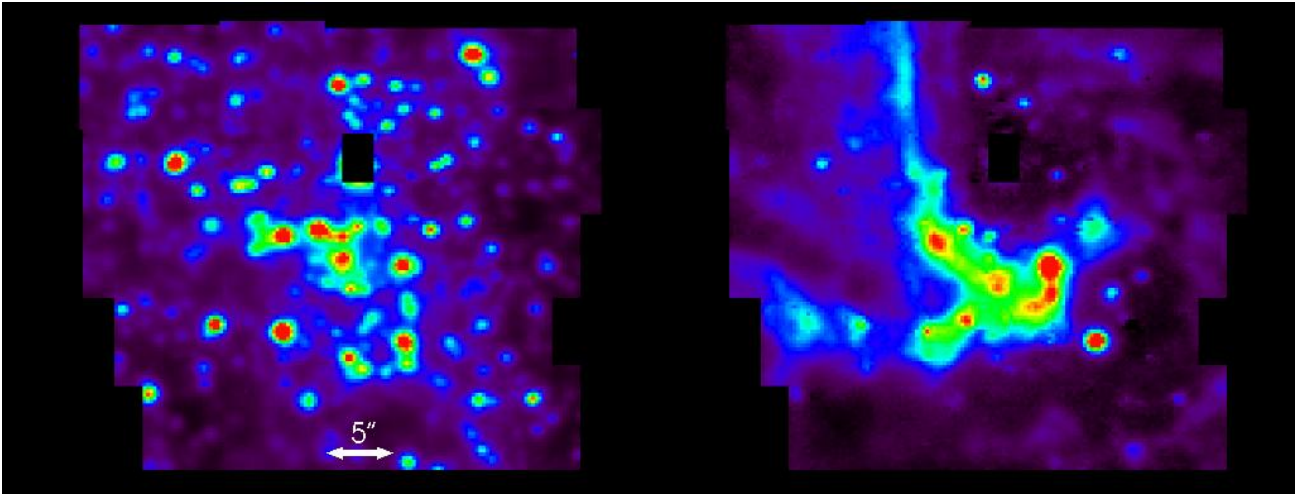


Figure 11. The minispiral in the Galactic Center: Continuum image around the $\text{Br}\gamma$ emission line at $2.166\mu\text{m}$ (left) and continuum subtracted, integrated $\text{Br}\gamma$ emission map (right) (both extracted from the H+K SPIFFI data cube).

A geometric determination of the distance to the Galactic Center: The distance between the Sun and the Galactic Center (R_0) is a fundamental parameter for determining the structure of the Milky Way through its impact on the calibration of the basic parameters of standard candles, such as RR Lyrae stars, Cepheids and giants. The determination of the distance to the Galactic Center has become possible through the advent of precision measurements of proper motions and line-of-sight velocities of the star S2 (see Figure 12), which is orbiting the massive black hole and compact radio source SgrA*. Our measurements reveal a Galactic Center distance of $R_0 = 7.94 \pm 0.52 \text{ kpc}$.

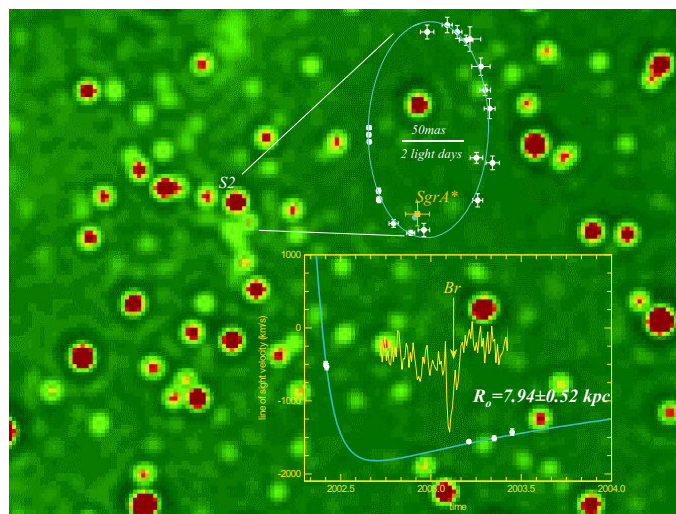


Figure 12. Geometric determination of the Sun-Galactic Center distance R_0 from a precision measurement of the orbital parameters of the star S2 that is orbiting the central supermassive black hole. The star's line-of-sight motion is measured via the Doppler shift of the $\text{Br}\gamma$ line in terms of an absolute velocity (SPIFFI data as well as spectroscopic data from NIRSPEC (Keck)¹¹ and from NACO), whereas its proper motion is measured in terms of an angular velocity (data from SHARP/NTT and NACO). The orbital solution ties the angular and absolute velocities, thereby yielding the distance to the S2/SgrA* binary system⁶.

REFERENCES

1. S. D. Lord, *NASA Techn. Memor. 103957*, 1992
2. H. Bonnet et al., *Proc. SPIE* **4839**, 2002
3. N. Devillard, "The eclipse software", *ESO Messenger* **87**, 1987
4. F. Eisenhauer et al., *Proc. SPIE* **4008**, 289, 2000
5. F. Eisenhauer et al., *Proc. SPIE* **4844**, 1548, 2003
6. F. Eisenhauer et al., *Ap.J.Letters* **597**, L121, 2003
7. G. Finger et al., "Comparison of Rockwell 1024×1024 MCT arrays science grade No. 2 and science grade No. 3", *internal ESO report*
8. J. D. Garnett, W. J. Forrest, *Proc. SPIE* **1946**, 395, 1993
9. R. Genzel et al., *MNRAS* **317**, 348, 2000
10. R. Genzel et al., *AP.J.* **564**, 633, 2003
11. A. Ghez et al., *Ap.J.Letters* **586**, L127, 2003
12. M. J. Horrobin et al., *AN* **325** 88, 2003
13. M. Meyer et al., "The ESO Infrared Detector High-Speed Array Control and Processing Electronics IRACE", *ESO Messenger* **86**, 1996
14. T. Ott et al., in preparation
15. J. Schreiber et al., *ASP Conference Series ADASS XIII*
16. M. Tecza et al., *Proc. SPIE* **4842**, 375, 2003